

# An Innovative Method to Determine Multi-System Performance for the Detection of Clandestine Tunnels

Carol Christou<sup>1</sup>, J. Casey Crager<sup>1</sup>, Landis Huffman<sup>1</sup>, Walter Kuklinski<sup>1</sup>, Eliot Lebsack<sup>1</sup>  
David Masters<sup>2</sup>, and Weiqun Shi<sup>1</sup>

<sup>1</sup>The MITRE Corporation  
Bedford, MA  
wshi@mitre.org

<sup>2</sup>The Department of Homeland Security, S&T  
Washington, D.C.

**Abstract**— The threat posed by underground clandestine tunnels has been a growing concern for law enforcement and national security. Cross-border tunnels have been used by smugglers with the intention of avoiding border security for trafficking people, drugs, firearms, and other illegal materials. The ability to detect these tunnels is vital to achieving effective border control. This paper describes the development of an innovative method to model and assess the performance of various sensor systems in the geological region of their intended use, and to determine the best sensing modalities and equipment to operate in that region.

The method includes: 1) Investigation and characterization of the regional representative geologic and geophysical properties of the shallow subsurface soil and environmental conditions along the southern US border; 2) Sensor performance modeling and simulation studies for various sensor system components/configurations, tunnel characteristics, surface and subsurface environmental and soil conditions; and 3) Validation and verification of the performance via tunnel detection testbed development and demonstration. The results of these combined efforts will be used to develop and implement an integrated sensor performance characterization suite to assist in identification of the most suitable methods and/or equipment to detect tunnels in a variety of locales.

A case study illustrating our approach applied to an area along the southern border using available field data to characterize the sensor performance indicates the methodology can yield accurate predictions of sensor performance in various geologies and at various levels of indigenous environmental noise. For the simulations to be useful, more work is planned to improve the accuracy of the sensor models, the precision of the geophysical databases, and to overcome the long execution times required for the models to run.

**Keywords**- tunnel detection, sensors, sensor performance, electromagnetic, GPR, seismic, homeland security, sensor fusion

## I. INTRODUCTION

The threat posed by underground clandestine tunnels has been a growing concern for law enforcement and national security. Cross-border tunnels have been used by smugglers to provide the means to move Weapons of Mass Destruction

(WMDs), drugs, conventional weapons, currency, and people across US borders illegally. Since 1990, there have been 154 illicit cross-border tunnels and numerous incomplete tunnels discovered along the southwest border. More than 50% of all the cross-border tunnels discovered to date have been found within the last four years. All cross-border tunnels mentioned above, with the exception of two, have been found by investigations and human intelligence. The development of a system to detect and locate cross-border tunnels is an enormous challenge. Traditional geophysical survey methods used primarily by the mining and oil and gas industries, as well as relatively newer non-destructive underground imaging and detection technologies, have not performed well. The inability to differentiate between tunnels and sub-surface clutter, and reject environmental noise continues to plague system developers in their pursuit of a suitable solution. That is not to say that all solutions are bad. Some systems may work in certain environments and certain geologies where the sensor is not overwhelmed by geological clutter and noise. This paper describes the development and use of a multi-sensor performance determination tool that considers local geology and environmental noise effects on the ability to detect and locate tunnels. Our intent is to use these methods and models as a physical basis to procure existing equipment that will have the best performance in the specific areas of interest and to identify research activities to improve the performance of existing methods or to identify new ones.

## II. SUBSURFACE GEOLOGICAL AND GEOPHYSICAL DATA

Subsurface geology and geophysics play a key role in sensor performance. Numerous studies highlighted the influence of environmental and geologic and geophysical properties on sensor performance and successful discrimination of tunnel signatures amid clutter [1]-[2]. The soil defines the contrast to a tunnel target, causes damping of electromagnetic or seismic waves, hence limiting the depth of investigation and creates geologic noise in the data that can mask the tunnel signal. Without a practical understanding of how the geology affects sensor response, the development of new high performance systems and the operation of existing techniques would be severely constrained.

This work is sponsored by the DHS S&T Contract HSHQDC-11-J-00219. Opinions and interpretations are those of the authors and are not necessarily endorsed by United States Government. Approved for Public Release; Distribution Unlimited. Case Number 12-3480.

The regional geological and geophysical conditions are quite diverse along the southwest border. Shallow subsurface characteristics range from basin-fill alluvium with unconsolidated sediments to weathered volcanic, granitic, metamorphic, and sedimentary rocks. Existing quantitative studies on sediment properties are scarce in the US border area, and the inventories of lithological and geotechnical properties of the sediments are generally not readily available. In order to develop physics-based sensor performance models, our first effort is to create a 3D subsurface geologic and geophysical database in areas having a high probability of where tunnels would be constructed. This is done by compiling data from open sources and conducting geophysical field surveys. We have developed and applied a multi-method approach to rapidly assess geophysical properties and hydrogeological conditions in areas that are geologically representative. This has led to a continuous shallow subsurface characterization model that describes the information on shallow subsurface geologic/geophysical strata, mineralogical composition, and key physical properties, such as electrical bulk conductivity, permittivity, density, and seismic velocities. Developing and expanding libraries of key physical properties and site characteristics will support optimized deployment strategies in high priority areas well in advance of the need to search for suspected targets. The database will be used to facilitate independent sensor design and response modeling and optimize sensor package, method selection, and field survey design.

### III. SENSOR SIMULATION TESTBED

A sensor simulation testbed has been developed to aid in the quantitative performance analysis of existing tunnel detection systems and to provide a mechanism to investigate both new and novel individual modalities applied to the tunnel detection problem. We have also developed the capability to quantify the potential of data fusion approaches that would utilize multiple modalities to enhance the detection of subsurface tunnels while also decreasing the probability of false alarms.

The testbed brings together information about the subsurface geology, numerical tools to predict the response of both active and passive sensor systems, a set of sensor performance quantification algorithms, and modeling and simulation tools that map existing subsurface physical characteristic data to the resolution required by the wave propagation algorithms used to predict the response of a given subsurface scenario to an applied source excitation.

A block diagram representation of the sensor simulation testbed is seen in Figure 1. In the testbed the user can specify a location of interest and tunnel configuration information including the tunnel cross section, size, depth, and orientation. As available, material characteristics from a subsurface data base are accessed for the location of interest. Presently, both electrical characteristics, including resistivity, permittivity, and permeability, and mechanical properties, such as density, seismic propagation velocities, compressional ( $V_p$ ) and shear

( $V_s$ ), and seismic attenuation factors ( $Q_p$  and  $Q_s$ ), are available in a large-scale subsurface database. To predict the response of a specified subsurface region to either an electromagnetic or seismic driving force, a variety of numerical wave propagation algorithms have been incorporated into the sensor simulation testbed. Since these wave propagation codes utilize the fundamental physics and phenomenology associated with the modalities under study, a very complete understanding of sensor performance and target signature response can be obtained. The effects of signal propagation in dispersive media, and resonances phenomena, along with multipath behavior, which are all important in subsurface propagation problems, are captured by the signal propagation methods employed in the Sensor Simulation Testbed. For wave propagation algorithms that use a finite-difference time-domain solution technique, the available geophysical data bases lack the necessary spatial resolution necessary to correctly calculate both electromagnetic and seismic energy propagation at the frequencies of interest for subsurface structures of tunnel size.

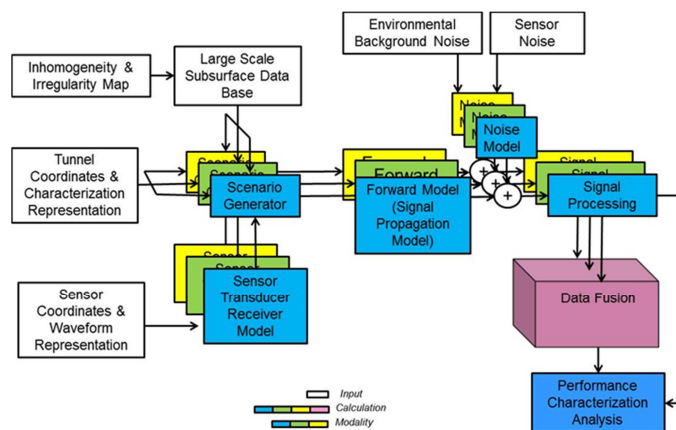


Figure 1: Sensor Simulation Testbed

The block labeled “Inhomogeneity and Irregularity Map” in Figure 1 represents a process for interpolation of the available geophysical data at any resolution to the resolution required by any specific numerical wave propagation algorithm. In cases where the geology of the region of interest is similar to a known geology, the interpolation is done using a Fractional Brownian motion model to generate multiple geologically plausible distributions of soil properties. Numerous studies [1]-[4] indicate subsurface irregularities have Fractal /Self-Similar character. Three-dimensional Fractional Brownian Motion (FBm) can be generated as a weighted integral of Gaussian White Noise. Representative subsurface models can be simulated using the FBm Power Law Power Spectral Density property. An isotropic 3D FBm subsurface model can be obtained by generating random Fourier phase spectra and using magnitude spectra consistent with a known or estimated Fractal Dimension. The power spectrum of FBm for a given Fractal dimension D is:

$$S(f_x, f_y, f_z) = G / (f_x^2 + f_y^2 + f_z^2)^{(2H+3)/2} \quad (0 < H < 1) \quad (1)$$

Where the Hurst parameter  $H = 0$  produces the roughest “subsurface texture” and  $H = 1$  produces the smoothest “subsurface texture”.  $H$  is related to the Fractal Dimension  $D$  and the Topological Dimension  $N$  as: Fractal Dimension  $D = N + 1 - H$ .  $G$  is a constant scale factor.

Non-isotropic subsurface textures can also be simulated by scaling the respective spatial frequencies as shown below for a two-dimensional (2D) case:

$$S(f_x, f_y) = G / \{ (f_x/\alpha)^2 + (f_y/\beta)^2 \}^{(2H+2)/2} \quad (2)$$

In equation (2),  $\alpha$  and  $\beta$  are parameters that specify the horizontal and depth correlation lengths, respectively. Representative two-dimensional subsurface textures generated using the FBM model are seen in Figure 2.

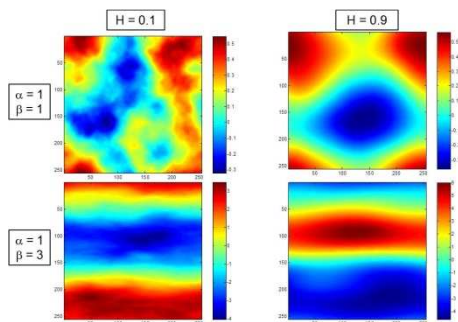


**Figure 2: Representative Two-Dimensional Subsurface Textures Generated using FBM**

The Sensor Simulation Testbed also includes the capability to evaluate a wide range of signal processing functions, including noise suppression and clutter mitigation. Detection methods ranging from Matched Filter processing for both monostatic and multistatic cases to adaptive statistical methods for clutter suppression have been implemented and can be readily refined to model any particular sensor system to a high degree of fidelity.

#### IV. NUMERICAL SIMULATION AND ANALYSIS CASE STUDIES

The following is a case study illustrating our simulation testbed approach to sensor system evaluation applied to an area along the southern border, using available field data to characterize the subsurface geology. Two simulation methods for EM-based GPR sensors were investigated. In the first, a horizontally stratified approximation of the subsurface geology was used in conjunction with an analytical plane wave propagation model. In this approach, the response for a GPR sensor operating in monostatic mode at a single location was simulated. The average resistivity and corresponding dielectric constant seen in Figure 4 were averaged in the lateral and depth dimensions to produce a three-layer horizontally stratified subsurface model. The resulting model had layer boundaries at 3 m and 23 m below the surface and a circular tunnel 3 m in diameter with its ceiling 12.5 m below the surface. The response to two cycles of a Hamming

weighted 200 MHz carrier was determined and used to calculate ROCs for a user specified background electromagnetic noise environment.

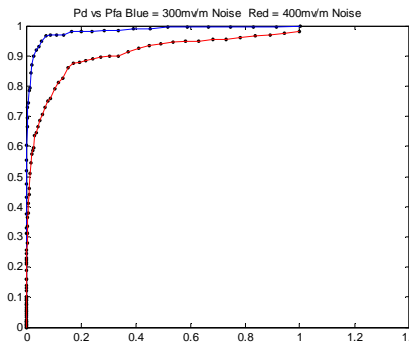


**Figure 3: Pd vs. Pfa for 200V/m Excitation at 300mV/m and 400mV/m Noise Levels.**

The resulting receiver operating characteristic (ROC) curves are seen in Figure 3 for background noise levels of 300mV/m (blue) and 400mV/m (red) noise levels.

In the second case study spatially varying two-dimensional resistivity and relative dielectric constant profiles were used as input to a two-dimensional FDTD electromagnetic propagation code.

#### A. FDTD GPR Simulation

We simulated operational ground-penetrating radar (GPR) by computing the propagation of an electromagnetic (EM) waveform pulse through the subsurface area of interest. Using measurements output from the simulation, we use a matched filter detection algorithm to locate potential tunnels. We subsequently characterized detection performance in the form of receiver operating characteristic ROC curves.

The surveyed measurements of resistivity and permittivity are leveraged to generate a two-dimensional representation of the EM properties of the subsurface at the survey location. The translation of surveyed measurements to a usable spatially discrete representation required additional processing. First, the FDTD numerical wave propagation code required finer spatial resolution resistivity data than those obtained by the survey. In this case, we use band-limited interpolation between surveyed data points to produce resistivity values on a grid at the resolution required by the simulation. Second, the survey did not provide more than a single permittivity value for the entire region. To produce permittivity values at higher resolution, we construct a model for the permittivity which leverages our knowledge of the region by using a mixture model of a matrix material (e.g. sand) and water, where the mixture component ratio varies spatially in proportion to the available resistivity data. Based on this mixture model, we construct a linear mapping from the finely sampled resistivity map to a permittivity map at the same resolution.

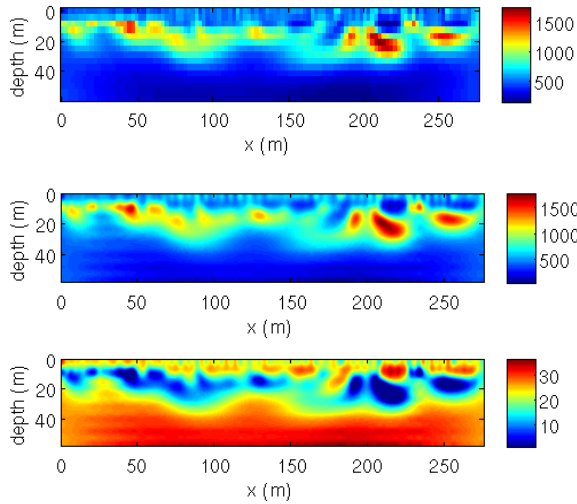


**Figure 4: (top) Raw surveyed resistivity data; (middle) Interpolated resistivity data; (bottom) Permittivity data derived from resistivity.**

The conversion from raw survey data to the simulated test medium is illustrated in Figure 4. We may simulate the presence of an underground tunnel by creating regions of air ( $\epsilon_r = 0$ ,  $\rho = \infty$ ) within the subsurface medium, as in Figure 5.

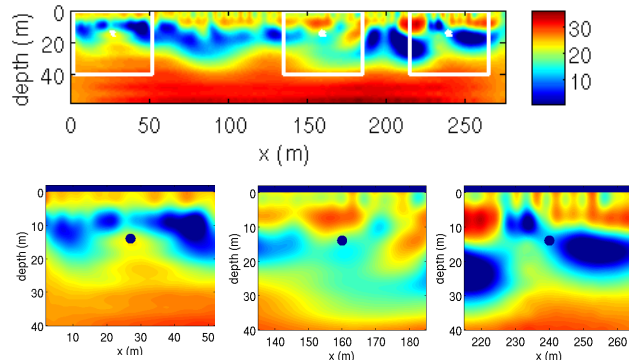


**Figure 5: Permittivity in simulated sub-regions: (top) Permittivity for survey region with simulated sub-regions indicated by white outline; (bottom row) permittivity within the three simulated regions – above-ground air layer and air-filled tunnel inserted into medium.**

EM wave propagation through the defined medium is simulated by obtaining a numerical solution to Maxwell's equations, using a staggered-grid finite-difference time domain (FDTD) approach [5] with perfectly matched layer (PML)-absorbing boundary conditions [6]. The FDTD method computes the strength of the 2D electric field components  $E_x$  and  $E_z$ , and of the magnetic field  $H_y$ .

We modeled both the transceiver antenna and resistive voltage source within our 2D EM FDTD framework. The basis for accounting for lumped linear and nonlinear circuit elements in electromagnetic FDTD modeling has been understood for many years. The key is to add the lumped electric current density of the circuit element to the total current in Ampere's Law when solving Maxwell's equations.

For a FDTD grid in the  $x$ - $y$  plane containing a resistive voltage source, the field components are defined on a standard Yee cell as shown in Figure 6. Here, the electric field vector components  $E_x$  and  $E_y$  are on the edges of the cell and the magnetic field component  $H_z$  is at the center of the cell.

For the edge containing the voltage source, a modified version of the standard FDTD update equation is used, as follows [7]:

$$E_{xi,j+1} = \beta E_{xi,j+1} - \frac{V_s}{\alpha \Delta x R_s} + \frac{1}{\alpha \Delta x} (H_{zi,j+1} - H_{zi,j}) \quad (4)$$

$$\text{Where: } \alpha = \frac{\epsilon}{\Delta t} + \frac{\sigma}{2} + \frac{1}{2R_s} \text{ and } \beta = \frac{1}{\alpha} \left( \frac{\epsilon}{\Delta t} - \frac{\sigma}{2} - \frac{1}{2R_s} \right).$$

Here  $\sigma$  is the electric conductivity,  $\epsilon$  is the dielectric constant,  $R_s$  is the internal source resistance,  $V_s$  is the source voltage, and  $\Delta t$  is the time step size.

Using this modified FDTD update relationship, a voltage source can be used to drive a dipole antenna. The dipole is modeled in 2D as two copper sheets separated by an air gap and extended to infinity in the  $\pm z$  directions. A user-defined voltage waveform can then be specified at the source location.

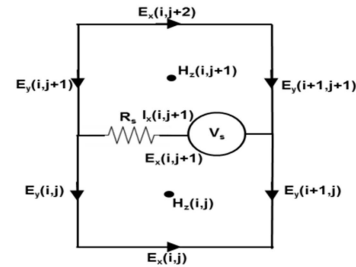


**Figure 6: Yee cell for resistive voltage source.**

Preliminary testing has been performed, using this 2D implementation for a 1 m dipole. For comparison, a 1 m bowtie antenna was designed using XFDTD (Commercial 3D electromagnetic FDTD software developed by Remcom, Inc.). Both simulations were performed in free-space with a 100 MHz Ricker waveform having 1-V peak amplitude. A snapshot of the  $E_x$  component of the electric fields at 20 ns for both the 3D and 2D simulations is shown in Figure 7. For the 3D case, the figure represents a planar slice through the center of the computational volume at the location of the bowtie antenna.

Qualitative inspection of Figure 7 indicates that both antennas radiate electric fields that are in agreement with those radiated by a typical dipole antenna. Notice also that beyond approximately 1 m distance from the antennas the fields are similar in shape, but different in amplitude. One possible explanation for this is that 2D and 3D waves are governed by different spreading-loss relationships. The 3D waves expand spherically; therefore their power density varies as  $1/r^2$ , where  $r$  is the distance from the antenna. On the other hand, 2D waves expand cylindrically and their power density varies as  $1/r$ . These spreading loss relations suggest that at a given distance from the antenna a spherical wave will experience a

higher degree of spreading loss than a cylindrical wave. This, however, needs to be explored in more detail.

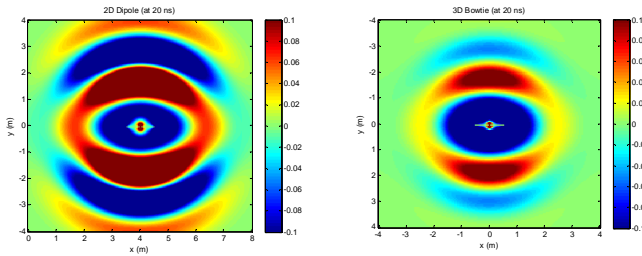


**Figure 7:  $E_x$  field at 20 ns for 2D dipole antenna (left) and 3D bowtie antenna (right).**

We simulate the operation of a GPR in three separate locations within the surveyed region, as indicated in Figure 5. In each simulation, we introduce a circular tunnel 3 m in diameter with a ceiling 12.5 m below the surface. The simulated GPR takes measurements every 0.5 m over a strip of ground 50 m long, centered over the top of the tunnel. We produce simulated radargrams,  $r(x,t)$ , from the measured voltages, as shown in Figure 8. The simulated radargrams indicate the influence that geological features have on GPR performance; namely, inhomogeneous permittivity results in wave reflections off permittivity boundaries. The clusters of low permittivity embedded in the soil visible in Figure 5 produce the strong parabolic returns in the radargrams seen in Figure 8. These returns due to soil inhomogeneity closely resemble the reflection from the tunnel, increasing the risk of false alarm for a GPR tasked with locating clandestine tunnels.

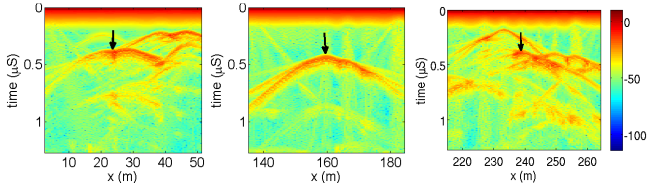


**Figure 8: Radargrams (colormap of voltages in dB) produced by GPR simulations in each of three locations. The arrow in each plot points to the top of the reflection due to the tunnel.**

While visual inspection of a simulated radargram gives a qualitative indication of its projected performance in the surveyed region, we aim to produce a quantitative measure of GPR performance. To accomplish this, we introduce an algorithm for detecting EM reflections from tunnels within the simulated radargrams. Our detection algorithm is an enhanced matched filter which compares the measured radargram to a collection of *hypothesized radargrams*,  $h_{x_0,z_0}(x,t)$ , which mimic the radargrams that *would have resulted* had a tunnel truly been present at each hypothesized location  $(x_0, z_0)$ . The inner product  $\langle r(x,t), h_{x_0,z_0}(x,t) \rangle$  provides a measure of similarity or match between the measured radargram  $r(x,t)$  and  $h_{x_0,z_0}(x,t)$ :

$$\langle r(x,t), h_{x_0,z_0}(x,t) \rangle = \iint r(x,t)h_{x_0,z_0}(x,t)dxdt. \quad (5)$$

Each hypothesized radargram  $h_{x_0,z_0}(x,t)$  can be produced using the simulation software – i.e. by introducing the tunnel at

location  $(x_0, z_0)$  in the synthetic medium and re-simulating the GPR. Since executing a GPR simulation at many hypothesized tunnel locations has very high computational demand, we propose a simplification to creating hypothesized radargrams. We begin by modeling the inhomogeneous medium in Figure 5 as homogenous with  $\rho$  and  $\epsilon_r$  set to the average surveyed values. Once the hypothesized radargram  $h_{x_0,z_0}(x,t)$  is produced for a tunnel at a single location in this homogenous medium, it is straightforward to use a physical propagation model to transform it into another hypothesized radargram  $h_{x_1,z_1}(x,t)$  resulting from the same tunnel at some other location  $(x_1, z_1)$  in the same homogenous medium:

$$h_{x_1,z_1}(x,t) \propto h_{x_0,z_0}(x', t + \Delta t), \quad (6)$$

where  $x' = x_0 + (z_0/z_1)(x - x_1)$ ,  $\Delta t = 2[\sqrt{(x' - x_0)^2 + z_0^2} - \sqrt{(x - x_1)^2 + z_1^2}]/v$ , and  $v$  is the constant velocity of wave propagation in the homogenous medium. Matching the simulated radargram to each of the hypothesized radargrams, we produce a matched filter-like response which may be thresholded to detect the presence or absence of tunnels, as shown in Figure 9. By sweeping the value of this threshold, we characterize the GPR performance in the form of a ROC curve. Note from the ROC curves in Figure 9 that the performance varies noticeably with location.

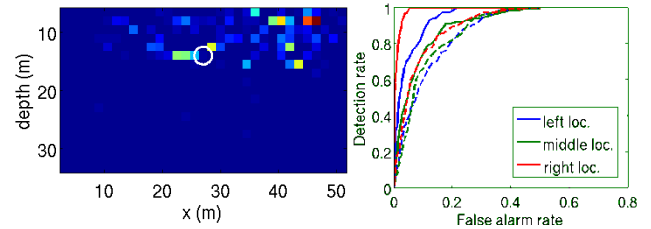


**Figure 9: (left) Matched filter response (with infinite SNR) at the leftmost simulation location (see Figure 5) with the true tunnel location outlined in white; (right) Resulting ROC curves at each of the three test locations using 200V/m excitation at noise levels of 1mV/m (solid) and 900mV/m (dashed).**

### B. Seismic Sensing Modality Simulation

A seismic wave produced by an active source on the ground will propagate through the soil until it reaches an interface between two media. There it will be partially transmitted and partially reflected. The reflection coefficient depends on the impedance mismatch between the two media, where impedance is the product of seismic phase velocity times the density of the soil. In the case of an air-filled void, the impedance mismatch will be very large, so that the seismic waves will be mostly reflected or critically refracted back to the surface, where they can be detected. This is mainly because the density of air is 1.2 kg/m<sup>3</sup>, at least 1000 times smaller than any solid medium, and the shear velocity is zero, since fluids cannot support shear strain. At the surface, the returned signal can be detected by multiaxial geophones recording the seismic particle velocity components. Active sources include weight drops, sledgehammers and explosions.

To date, most of our simulations have been based on the FDTD software package E3D, which originated at Lawrence Livermore National Laboratory (LLNL) [8]. We also have a similar package developed by the MIT Earth Resources Laboratory (MIT ERL). The inputs to the numerical codes include  $V_p$ ,  $V_s$ ,  $\rho$  and the attenuation factors  $Q_p$  and  $Q_s$  of the subsurface media. In addition to geometrical spreading, seismic waves invariably suffer attenuation as they propagate through a medium. The attenuation is an exponentially decreasing function of frequency. Higher frequencies are therefore attenuated more. Various types of sources may be specified along with a user-defined waveform. For our application, we typically specify either a vector force or moment tensor at the surface. So far, we have primarily used a Ricker wavelet to represent the input driving force. Simulation outputs include pressure, and the  $x$ ,  $y$ , and  $z$  velocity components  $v_x$ ,  $v_y$ , and  $v_z$  at any depth. The code requires a time-step that satisfies the Courant condition, which states that the time sampling  $dt$  must be small enough that the longest wavelengths, propagating at the highest velocity  $V_{max}$ , do not outrun the spatial grid sampling  $dh$ :  $dt < factor \cdot dh/V_{max}$ , where the factor constant is 0.606 for 2D problems and 0.494 for 3D problems.

A simple example is shown in Figure 10. This geometry represents a cross-section of a homogeneous 3D volume containing a rectangular air-filled tunnel. The material properties for this subsurface are  $V_p = 268.7$  m/s,  $V_s = 164.5$  m/s, and  $\rho = 1570$  kg/m<sup>3</sup>, no attenuation, and the tunnel itself was assigned the following properties for air:  $V_p = 332$  m/s,  $V_s = 0$  m/s, and  $\rho = 400$  kg/m<sup>3</sup>. Although the density of air is  $\sim 1.2$  kg/m<sup>3</sup>, the higher value is required for numerical stability and does not affect the fidelity of the results. A 100 Hz Ricker pulse was applied directly above the tunnel at the midpoint of the upper surface of a computational volume equal to 50x20x20 m<sup>3</sup>, as indicated in the figure. The resolution for all simulations was 10 cm in each direction. Seismic wave pressure and velocity were then recorded every 0.2 m along the 50 m length of the test volume. The resulting seismogram for the compressional velocity  $z$  component is shown in the figure obtained from the output of E3D using the open source collection of seismic processing MATLAB toolbox, SeisLab, [9]. We notice two linear envelopes, the outer one arising from the directly received compressional wave and the inner one from the Rayleigh surface wave. The hyperbolic-shaped returned wave fronts due to the tunnel can be clearly distinguished and are contained within the inner envelope.

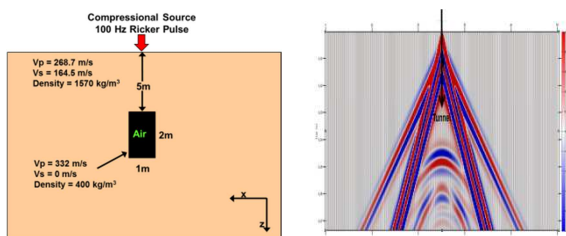


**Figure 10: Cross-section of homogeneous 3D subsurface simulation geometry (left) and the simulated seismograms of  $V_z$  produced by E3D and SeisLab codes (right).**

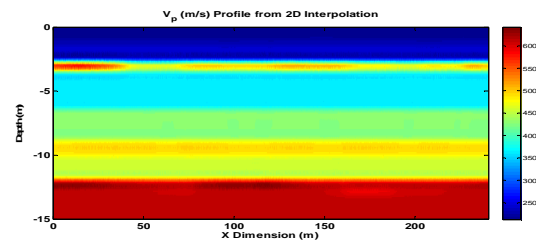


**Figure 11: Profile of  $V_p$  after interpolation into field data.**

Figure 11 is a 2D 10 cm resolution image plot of  $V_p$ , obtained by interpolation of coarser field data collected along a site in the southern border. We notice the presence of subsurface inhomogeneities and inversion layers, which may cause interference with the tunnel signal. Similar interpolations were effected to produce 2D inputs for  $V_s$ ,  $Q_p$  and  $Q_s$ , while  $\rho$  was obtained from  $V_p$  through an empirical relationship,  $\rho = 0.2714V_p + 1192.9$  in kg/m<sup>3</sup> [10]. Figure 12 is a seismogram corresponding to the presence of a similar tunnel as in Figure 10 for this more realistic profile, in the absence of attenuation. Here, the received signals form a more complex pattern because of the inhomogeneous nature of the subsurface. This can be better understood from the E3D snapshots of the propagating wave fronts for the homogeneous and the inhomogeneous media in Figure 13. The wave fronts are color coded, so that red hues correspond to P waves and green hues to S waves. In the left plot we clearly see the first-arrival P waves, which form the outer envelope of the seismogram in Figure 12, and the Rayleigh waves, which form the inner envelope and appear as white blips along the surface. We also notice the generation of P wave resonances, as well as the absence of S waves, within the tunnel. In the lower plot, the pattern is more complex, due to inhomogeneities, which may cause reflections from lower strata or the tunnel to arrive at a sensor position before the initial P wave. While the results shown here provide a qualitative indication of seismic performance, we have also developed a tunnel detection scheme based on a matched filter approach to provide a quantitative measure of performance analogous to the EM effort described earlier.

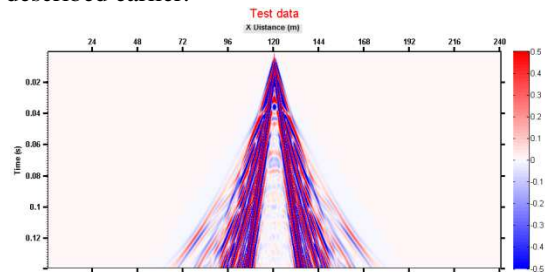


**Figure 12: Seismogram of  $V_z$  at Surface for a 1mX2m tunnel buried at 5m deep. .**

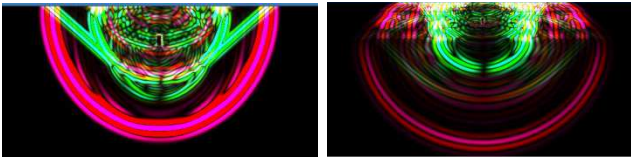


**Figure 13: Snapshots of propagation of seismic waves for: Tunnel in homogeneous medium (left) and tunnel in inhomogeneous medium (right).**

## V. SYSTEM INTEGRATION

The block diagram as shown in Figure 14 is largely implemented using the MATLAB analysis scripting language. MATLAB is especially useful for this purpose due to the breadth of graphical user interface (GUI) components offered as well as the availability of a compiler toolchain to facilitate deployment on analysis workstations.

The left-to-right flow of data through the key components in Figure 14 provides a basis for GUI design. As this flow is independent of sensor modality, a common framework has been developed which relies on abstraction to tie all of the disparate modalities together into a single unified GUI structure. Working from left to right, the subsurface database is composed of a series of binary files, each of which contain a single geophysical constitutive parameter. The user selects a subset of the overall database through a map-like interface (a point, click, and drag operation); the underlying scripts will extract the desired subset from the subsurface database through interpolation. Figure 14 illustrates a subset of a geophysical database for an area of interest. The subset can be viewed and augmented with synthetic targets (e.g. boulders, pipes, and tunnels) to provide a scenario data set.

Once the scenario is defined, the sensor *modality* and *implementation* must be selected. Electromagnetic and seismic modalities are currently defined, but this is not an exhaustive list. Within these modality families, specific forward models, or implementations, (e.g. 2D/3D electromagnetic FDTD for GPR simulation) are available for selection and definition. The scenario data set is then converted into a form most suitable for the implementation. Depending on the modality, one or more sensors are then placed by the user into the scenario data set. The orientation, excitation waveform, and other relevant parameters are associated with each sensor, and carried along into the forward model simulation.

The forward model simulation is executed either as a self-contained MATLAB code (for simpler implementations), or as a directed system call to an external application suite. In either case, the architecture must ensure that all inputs are in a form understandable to the forward model code. The forward model is executed to provide a noise-free signal.

The uncorrupted signal produced by the forward method is the basis upon which a desired noise model may be superimposed. The noise model most suitable for each modality is defined through user input as a step before signal processing analysis is performed. Signal processing methods commonly employed for each modality are implemented to help assess the achievable performance that may be achieved for a given

modality. Among the more common metrics, SNR and  $P_d$  may be computed, as well as complete Receiver Operating Curves (ROC) that may be used to help differentiate sensor modalities for a given subsurface scenario.

MATLAB executes internal code synchronously, so forward models implemented in this manner will block the GUI interface until the forward model completes execution. Forward models implemented using external codes may be executed in parallel, which requires additional code to periodically check the status of the forward model execution.

## VI. CONCLUSION

The development of a physics-based approach to clandestine tunnel detection is necessary to estimate system performance, identify shortfalls in existing technologies, and make productive investments in research and development. Based on effects of subsurface complexity on discriminating tunnels from clutter, work will continue with the geological field collections, as will sensor and geophysical modeling of the specific areas where the equipment will be operated.

## ACKNOWLEDGMENT

We would like to thank Dr. John Lane and Carol Johnson from USGS Office of Groundwater in Storrs, CT, and Dr. Rich Miller from Kansas Geological Survey, for providing field data. We also give special thanks to Colin Shellum and Steve Nicely from DTRA's HTRAC Geotechnical Team for providing geological models.

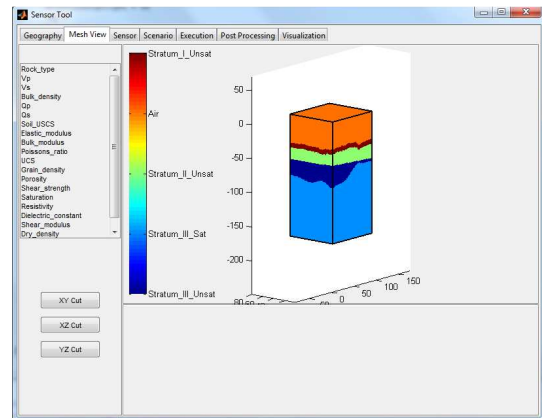


**Figure 14: Scenario Data Set Visualization Feature**

## REFERENCES

- [1] Benjamin T. Richards, Don Steeples, Rick Miller, Julian Ivanov, Shelby Peterie, Steven D. Sloan, and Jason R. McKenna, Near-surface shear-wave velocity measurements in un lithified sediment, SEG Expanded Abstracts 30, 1416, 2011,
- [2] Jose L. Llopis, Joseph B. Dunbar, Lillian D. Wakeley, Maureen K. Corcoran, Dwain K. Butler, Tunnel Detection Along The Southwest U.S. Border, SAGEEP, Extended abstract, April 2005,
- [3] Correlation length and fractal dimension interpretation from seismic data using variograms and power spectra., Ken Mela and John N. Louie, GEOPHYSICS, Vol. 66, No. 5 (September-October 2001); P. 1372–1378,

- [4] Mapping soil fractal dimension in agricultural fields with GPR, K. Oleschko, G. Korvin, A. Muñoz, J. Velazquez, M. E. Miranda, D. Carreon, L. Flores, M. Martínez, M. Velásquez-Valle, F. Brambila, J.-F. Parrot, and G. Ronquillo, *Nonlin. Processes Geophys.*, 15, 711–725, 2008.
- [5] K. Yee, “Numerical solution of initial boundary value problems involving Maxwell’s equations in isotropic media,” *IEEE Transactions on Antennas and Propagation* vol. 14 (3), pp. 302-307.
- [6] J. Berenger, “A perfectly matched layer for the absorption of electromagnetic waves,” *Journal of Computational Physics*. Vol 114 (2), pp. 185–200.
- [7] W. Sui, D. A. Christensen, and C. H. Durney, “Extending the Two-Dimensional FDTD Method to Hybrid Electromagnetic Systems with Active and Passive Lumped Elements,” *IEEE Trans. Microwave Theory Tech.*, vol. 40, no. 4, pp. 724–730, April 1992.
- [8] E3D: 2D/3D Elastic Finite-Difference Wave Propagation Code, Shawn Larsen, Lawrence Livermore National Laboratory, <http://crack.seismo.unr.edu/ftp/pub/louie/class/455/e3d/e3d.txt>.
- [9] SeisLab for MatLab, MATLAB Software for the Analysis of Seismic and Well-Log Data. A Tutorial, Eike Rietsch, Version 3.01, February 14, 2010.
- [10] Seismic Propagation Modeling, Stephen Ketcham, U.S. Army Engineer Research and Development Center, Hanover, NH, February 2011.